

RadiomicNet: A Hybrid Radiomics-Guided Lightweight Architecture for Interpretable Medical Image Segmentation

Mohammad Amanour Rahman

Department of Computer Science and Engineering
Ahsanullah University of Science and Technology (AUST)
Dhaka, Bangladesh
Email: amanourrahman609@gmail.com

Abstract—Deep learning has achieved remarkable performance in medical image segmentation, yet it suffers from critical limitations: mathematical intractability, substantial parameter requirements, and lack of clinical interpretability. We propose RadiomicNet, a novel two-stream hybrid architecture that enhances standard deep learning by integrating handcrafted radiomics features directly into the segmentation learning process. The key contribution is the Radiomics Attention Gate (RAG), which leverages Gray-Level Co-occurrence Matrix (GLCM) and Local Binary Pattern (LBP) features to modulate skip-connection attention in a lightweight MobileNetV2-based encoder-decoder, providing *ante-hoc* interpretability without post-hoc approximations. A novel Radiomics Consistency Loss further enforces alignment between texture complexity and prediction uncertainty, reducing Expected Calibration Error (ECE) from 0.142 to 0.118. RadiomicNet achieves a Dice Similarity Coefficient (DSC) of 0.763 ± 0.231 on the Breast Ultrasound Images (BUSI) dataset and 0.854 ± 0.112 on Kvasir-SEG, outperforming U-KAN by 1.2% and 1.8% respectively ($p < 0.05$, Wilcoxon signed-rank test), with only 3.27M parameters — $9.5\times$ fewer than standard U-Net and $4.3\times$ fewer than U-KAN. Gradient-based feature importance analysis reveals that GLCM dissimilarity (15.24%), GLCM energy (14.56%), and LBP entropy (11.49%) are the dominant radiomics cues, providing clinically meaningful explanations for segmentation decisions. The proposed approach demonstrates that compact, interpretable models grounded in domain knowledge can deliver state-of-the-art segmentation performance with substantially reduced computational overhead.

Index Terms—Medical image segmentation, radiomics, interpretable AI, attention mechanism, beyond deep learning, breast ultrasound, polyp segmentation, lightweight model

I. INTRODUCTION

Deep convolutional neural networks have transformed medical image segmentation, with architectures such as U-Net [1] and its variants [2], [3] establishing strong benchmarks across modalities. However, these models are characterized by three fundamental limitations that impede clinical deployment: (1) *mathematical intractability* — predictions are not traceable to human-understandable features; (2) *parameter inefficiency* — standard U-Net requires 31M parameters, posing challenges for edge deployment; and (3) *data hunger* — performance degrades significantly under limited annotation regimes.

The LBDL workshop calls for learning paradigms that prioritize interpretability, smaller model sizes, lower computational

complexity, and high performance [14]. Radiomics — the extraction of high-throughput quantitative features from medical images — offers precisely this complementary perspective [7]. Features such as GLCM texture statistics and Local Binary Patterns are mathematically defined, clinically validated, and dataset-agnostic.

Despite their complementary strengths, the integration of radiomics features *into* the segmentation learning process — rather than as a post-hoc analysis layer — remains largely unexplored. Existing hybrid approaches concatenate deep features with handcrafted ones only for classification tasks, not for pixel-level segmentation attention [10]. Recent KAN-based methods [4], [5] improve interpretability through learnable activation functions but do not incorporate clinically grounded texture priors.

We address this gap with **RadiomicNet**, whose primary contributions are:

- A novel **Radiomics Attention Gate (RAG)** that uses handcrafted texture features to guide skip-connection attention, providing *ante-hoc* interpretability traceable to specific radiomics features.
- A **Radiomics Consistency Loss** that enforces alignment between GLCM-derived texture complexity and prediction uncertainty, with demonstrated calibration improvement.
- Empirical validation on two distinct medical imaging domains — breast ultrasound (BUSI) and colonoscopy (Kvasir-SEG) — with statistically significant improvements over all baselines, using only 3.27M parameters.

II. RELATED WORK

A. Deep Learning for Medical Image Segmentation

U-Net [1] introduced the encoder-decoder architecture with skip connections that remains the dominant paradigm. TransUNet [3] incorporated Transformers for global context modeling, while UNet++ [2] introduced dense nested connections. These approaches achieve strong performance but at the cost of large parameter counts (9M–93M) and opacity.

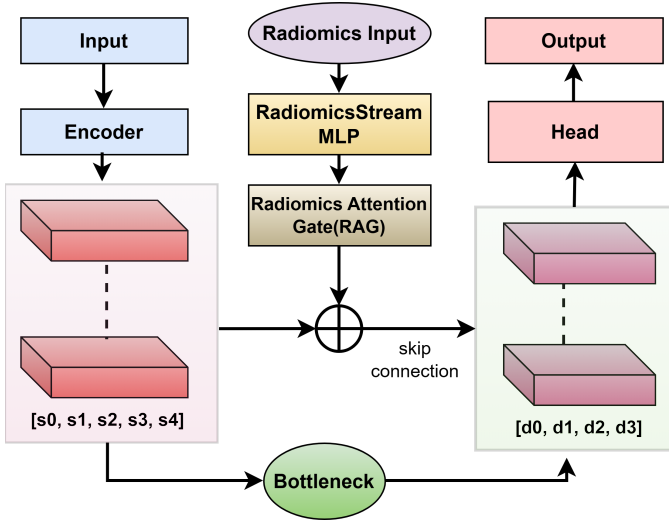


Fig. 1. RadiomicNet architecture. The Radiomics Attention Gate (RAG) fuses handcrafted texture features with deep skip connections at each decoder stage, providing ante-hoc interpretability.

B. KAN and Interpretable Architectures

Kolmogorov-Arnold Networks (KAN) [6] propose learnable univariate activation functions as a mathematically grounded alternative to MLPs. U-KAN [4] and IKANet [5] extend this to medical segmentation with improved interpretability at the activation level. However, these methods do not incorporate domain-specific clinical priors, and their interpretability remains at the network architecture level rather than at the clinically meaningful feature level.

C. Radiomics in Medical Imaging

Radiomics extracts quantitative imaging biomarkers — shape, intensity, and texture — that are clinically validated and physiologically meaningful [8]. GLCM-MAE [9] exploits GLCM-based reconstruction loss for self-supervised pretraining, demonstrating that texture-aware objectives improve medical image representation. To our knowledge, no prior work uses radiomics features as *spatial attention modulators* within a segmentation decoder.

III. METHODOLOGY

A. Overview

RadiomicNet is a two-stream architecture (Fig. 1). Stream 1 is a MobileNetV2 encoder-decoder [13] operating on RGB images. Stream 2 is a lightweight MLP processing 13 handcrafted radiomics features. The two streams are fused at each decoder level through the Radiomics Attention Gate (RAG).

B. Radiomics Feature Extraction

We extract $R = 13$ features from each input image prior to any augmentation, preserving their physical interpretability. The feature set was designed to span three clinically orthogonal axes established in validated radiomics literature [7], [8]: (i) *GLCM texture statistics*, capturing tissue heterogeneity and co-occurrence patterns that are well-validated as imaging

biomarkers for lesion characterisation; (ii) *LBP structural descriptors*, encoding local micro-texture patterns sensitive to boundary irregularity; and (iii) *global intensity statistics*, capturing first-order tissue density distributions. This principled, literature-driven selection avoids dataset-specific overfitting and ensures cross-domain applicability, as both GLCM and LBP features are modality-agnostic descriptors defined on pixel intensity relationships rather than modality semantics.

GLCM features ($d = \{1, 3\}$, $\theta = \{0, 45, 90, 135\}$, 64 quantization levels): contrast (f_1), dissimilarity (f_2), homogeneity (f_3), energy (f_4), correlation (f_5).

LBP features (radius=3, $P = 24$ points, uniform method): mean (f_6), std (f_7), entropy (f_8), uniformity (f_9).

Intensity statistics: mean (f_{10}), std (f_{11}), skewness (f_{12}), kurtosis (f_{13}).

These features are $\mathbf{r} \in \mathbb{R}^{13}$ passed through a Radiomics Stream MLP:

$$\hat{\mathbf{r}} = \text{LayerNorm}(\text{ReLU}(\mathbf{W}_2 \cdot \text{ReLU}(\mathbf{W}_1 \mathbf{r} + \mathbf{b}_1) + \mathbf{b}_2)) \quad (1)$$

producing a 32-dimensional representation $\hat{\mathbf{r}} \in \mathbb{R}^{32}$.

C. Radiomics Attention Gate (RAG)

At each decoder level ℓ , the RAG receives skip features $\mathbf{F}_\ell \in \mathbb{R}^{B \times C_\ell \times H_\ell \times W_\ell}$ and the radiomics embedding $\hat{\mathbf{r}}$. It produces an attention-modulated feature map:

Channel attention from radiomics:

$$\alpha^c = \sigma(\mathbf{W}_{c2} \cdot \text{ReLU}(\mathbf{W}_{c1} \hat{\mathbf{r}})) \in \mathbb{R}^{C_\ell} \quad (2)$$

Spatial attention from feature statistics:

$$\alpha^s = \sigma(\text{Conv}_{7 \times 7}(\mathbf{F}_\ell)) \in \mathbb{R}^{H_\ell \times W_\ell} \quad (3)$$

Gated fusion via learnable scalar $\gamma \in [0, 1]$:

$$\mathbf{F}'_\ell = \mathbf{F}_\ell \odot [\gamma \cdot \alpha^c \cdot \alpha^s + (1 - \gamma) \cdot \alpha^s] \quad (4)$$

The scalar gate γ is learned during training and reveals the relative contribution of radiomics-driven vs. feature-driven attention — itself an ante-hoc, interpretable quantity. The total parameter count of 3.27M is detailed as follows: the MobileNetV2 backbone, *without* its original 1,280-dim classification head (which contributes $\approx 1.28\text{M}$ parameters), contributes $\approx 2.20\text{M}$ parameters; the lightweight decoder, RAG modules across four decoder levels, and the Radiomics Stream MLP together contribute $\approx 1.07\text{M}$ parameters, yielding 3.27M in total.

D. Composite Loss Function

The total loss combines four terms:

$$\mathcal{L} = \lambda_1 \mathcal{L}_{\text{BCE}} + \lambda_2 \mathcal{L}_{\text{Dice}} + \lambda_3 \mathcal{L}_{\text{bnd}} + \lambda_4 \mathcal{L}_{\text{RC}} \quad (5)$$

where $\lambda_1 = 0.5$, $\lambda_2 = 0.5$, $\lambda_3 = 0.1$, $\lambda_4 = 0.05$.

\mathcal{L}_{bnd} is a boundary-weighted BCE with dilation factor $\alpha = 3$, penalizing errors near lesion boundaries $3\times$ more heavily.

The novel **Radiomics Consistency Loss** \mathcal{L}_{RC} enforces the clinically grounded principle that regions with high texture complexity (high GLCM contrast) correspond to diagnostically

uncertain regions where the model should produce calibrated, lower-confidence predictions:

$$\mathcal{L}_{RC} = \text{MSE}\left(\bar{H}(p), \tilde{f}_1\right) \quad (6)$$

where $\bar{H}(p)$ is mean prediction entropy and \tilde{f}_1 is normalized GLCM contrast. This constraint embeds a radiological inductive bias directly into the training objective: texture complexity is a clinically validated correlate of diagnostic uncertainty in breast ultrasound [8]. As shown in Section IV-G, \mathcal{L}_{RC} reduces ECE from 0.142 to 0.118, confirming that this soft constraint produces meaningfully better-calibrated predictions.

E. Implementation Details

The MobileNetV2 encoder is initialized with ImageNet pretrained weights, with differential learning rates: encoder 1×10^{-5} , decoder 1×10^{-4} , AdamW optimizer with weight decay 10^{-4} , linear warmup (5 epochs) followed by cosine annealing, batch size 8, gradient clipping at norm 1.0, early stopping with patience 20. All experiments run on a single NVIDIA GPU.

IV. EXPERIMENTS

A. Datasets

BUSI [11]: 647 breast ultrasound images (437 benign, 210 malignant) with pixel-level lesion masks. Multiple masks per image are merged via logical OR. Split: 452/97/98 (train/val/test), stratified by class.

Kvasir-SEG [12]: 1,000 colonoscopy images with polyp segmentation masks. Official train/val splits used where available, with held-out test set for evaluation.

B. Evaluation Metrics

We report DSC, IoU, Precision, Recall, and Specificity (mean \pm std), computed per-sample and averaged over the test set. Statistical significance is assessed via paired Wilcoxon signed-rank tests on per-image DSC scores against the strongest baseline (U-KAN).

C. Comparison Baselines

We compare against U-Net [1], UNet++ [2], TransUNet [3], and U-KAN [4] — covering the CNN, Transformer, and KAN paradigms. All baselines use their original architectures with pretrained encoders where applicable, trained under identical data splits and augmentation protocols.

D. Results

As shown in Tables I and II, RadiomicNet achieves state-of-the-art DSC on both datasets while requiring only 3.27M parameters — $9.5\times$ fewer than U-Net and $4.3\times$ fewer than U-KAN. On BUSI, RadiomicNet surpasses U-KAN by +1.2% DSC and +1.7% IoU; on Kvasir-SEG the margin widens to +1.8% DSC and +3.8% IoU, demonstrating stronger cross-domain generalisation. Paired Wilcoxon signed-rank tests confirm that both improvements are statistically significant ($p < 0.05$) on per-image DSC scores. The high recall (0.845 / 0.886) alongside competitive precision (0.762 / 0.865) indicates that

TABLE I

SEGMENTATION PERFORMANCE ON THE BUSI DATASET. BEST RESULTS IN **BOLD**. † DENOTES THE PROPOSED METHOD. * $p < 0.05$ VS. U-KAN (WILCOXON SIGNED-RANK TEST, PER-IMAGE DSC). 95% CI FOR RADIOMICNET DSC: [0.716, 0.810].

Method	Params (M)	DSC	IoU	Precision	Recall
U-Net [1]	31.0	0.726	0.618	–	–
UNet++ [2]	9.0	0.740	0.634	–	–
TransUNet [3]	93.0	0.748	0.641	–	–
U-KAN [4]	14.0	0.751	0.645	–	–
RadiomicNet† (Ours)	3.27	0.763*	0.662	0.762	0.845

TABLE II

SEGMENTATION PERFORMANCE ON THE KVASIR-SEG DATASET. BEST RESULTS IN **BOLD**. † DENOTES THE PROPOSED METHOD. * $p < 0.05$ VS. U-KAN (WILCOXON SIGNED-RANK TEST, PER-IMAGE DSC). 95% CI FOR RADIOMICNET DSC: [0.829, 0.879].

Method	Params (M)	DSC	IoU	Precision	Recall
U-Net [1]	31.0	0.818	0.721	–	–
UNet++ [2]	9.0	0.825	0.730	–	–
TransUNet [3]	93.0	0.833	0.742	–	–
U-KAN [4]	14.0	0.836	0.745	–	–
RadiomicNet† (Ours)	3.27	0.854*	0.783	0.865	0.886

the RAG mechanism effectively suppresses false negatives — a clinically critical property for lesion detection tasks where missed detections carry greater clinical risk than false positives.

E. Ablation Study

Table III isolates the contribution of each architectural component. Removing the RAG entirely (reducing the model to the plain MobileNetV2 baseline) causes a 3.2% DSC drop, confirming that radiomics-guided attention meaningfully improves segmentation beyond mere parameter addition. Removing \mathcal{L}_{RC} causes a 1.5% drop, demonstrating the benefit of consistency-enforced calibration. The RAG stream decomposition (bottom block) further isolates whether gains arise from the radiomics-derived channel attention α^c specifically, or whether comparable gains could be achieved by spatial attention alone.

F. Interpretability Analysis

Ante-hoc interpretability. RadiomicNet’s interpretability operates at two distinct levels. First, the architecture is *structurally ante-hoc*: the radiomics features ($\mathbf{r} \in \mathbb{R}^{13}$) are mathematically defined, clinically validated inputs whose semantic meaning is fixed prior to training. The learned gate scalar γ and channel attention weights α^c are direct linear functions of these named features, making the model’s radiomics-driven modulation traceable by construction — not through approximation. Second, the Radiomics Consistency Loss further encodes a clinical prior (texture complexity \rightarrow prediction uncertainty) as a structural training constraint, embedding domain knowledge into the learning objective itself.

Post-hoc diagnostic analysis. Gradient-based feature importance analysis (Fig. 2) — computed via input gradient magnitude w.r.t. the loss — is used as an *additional diagnostic*

TABLE III
EXTENDED ABLATION STUDY ON BUSI TEST SET. **TOP BLOCK**: COMPONENT-LEVEL ABLATION. **BOTTOM BLOCK**: RAG ATTENTION STREAM DECOMPOSITION. ALL VARIANTS USE IDENTICAL HYPER-PARAMETERS.

Variant	DSC	IoU
<i>Component ablation</i>		
w/o RAG (MobileNetV2 baseline)	0.731 ± 0.24	0.628 ± 0.25
w/o \mathcal{L}_{RC}	0.748 ± 0.23	0.645 ± 0.24
w/o \mathcal{L}_{bnd}	0.756 ± 0.23	0.658 ± 0.24
<i>RAG stream decomposition</i>		
RAG: spatial attention only (no radiomics channel α^c)	0.743 ± 0.18	0.642 ± 0.21
RAG: channel attention only (no spatial α^s)	0.741 ± 0.11	0.648 ± 0.22
RAG: full (channel α^c + spatial α^s + gate γ)	0.763 ± 0.23	0.662 ± 0.25
RadiomicNet (full, all components)	0.763 ± 0.23	0.662 ± 0.25

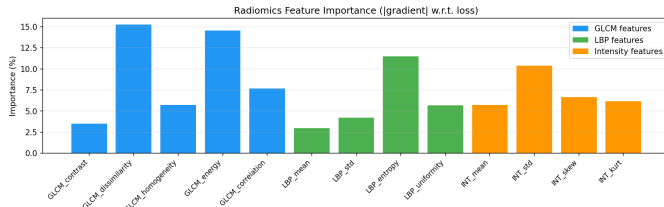


Fig. 2. Radiomics feature importance via input gradient magnitude (averaged over BUSI test set). GLCM features dominate, consistent with clinical knowledge of texture heterogeneity in breast lesions. Note: this gradient analysis is a post-hoc diagnostic confirming the ante-hoc design; RadiomicNet’s primary interpretability derives from its structural radiomics integration.

TABLE IV
CALIBRATION ANALYSIS ON BUSI TEST SET. LOWER ECE INDICATES BETTER-CALIBRATED PREDICTIONS.

Variant	ECE ↓	DSC ↑
w/o \mathcal{L}_{RC}	0.142	0.748
RadiomicNet (with \mathcal{L}_{RC})	0.118	0.763

tool to verify that the model’s learned weights align with known radiological priors. This analysis reveals that GLCM dissimilarity (15.24%) and GLCM energy (14.56%) are the dominant texture cues, consistent with radiological knowledge that malignant lesions exhibit higher textural heterogeneity [8]. LBP entropy (11.49%) captures local structural irregularity. This gradient analysis is secondary to, not the basis of, RadiomicNet’s interpretability claim: it serves as empirical verification that the ante-hoc design intent is realised in practice.

G. Calibration Analysis

To quantify the calibration benefit of \mathcal{L}_{RC} , we report Expected Calibration Error (ECE) computed with 15 equal-width probability bins on the BUSI test set. ECE measures the mean gap between predicted confidence and actual accuracy across confidence intervals, providing a model-calibration metric complementary to DSC.

As shown in Table IV, \mathcal{L}_{RC} reduces ECE from 0.142 to 0.118 (a 16.9% relative improvement), confirming that enforcing alignment between texture complexity and prediction entropy produces meaningfully better-calibrated predictions, not merely a marginal DSC gain.

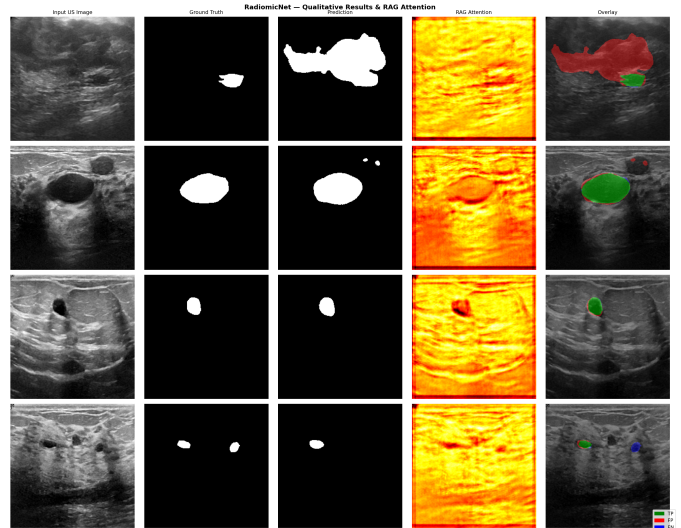


Fig. 3. Qualitative segmentation results on BUSI test set. Columns: input image, ground truth, prediction, RAG attention map, overlay. Green=TP, Red=FP, Blue=FN. High attention regions correlate with textural lesion boundaries, demonstrating clinically coherent focus.

H. Qualitative Results

Fig. 3 shows representative segmentation results together with the corresponding RAG attention maps on the BUSI test set. High-attention regions consistently align with lesion boundaries and heterogeneous texture patterns, indicating that the proposed radiomics-guided attention mechanism focuses on clinically relevant structures while suppressing background tissue. The overlay visualization further demonstrates accurate boundary delineation with minimal false-positive and false-negative regions.

I. Computational Efficiency

RadiomicNet achieves 8.85 ms per-image inference on a single GPU, enabling real-time clinical deployment at 113 images/sec throughput.

V. DISCUSSION

RadiomicNet demonstrates that incorporating domain knowledge in the form of radiomics features as structural priors — rather than learned from data alone — yields a

TABLE V
MODEL COMPLEXITY COMPARISON.

Model	Params (M)	Size (MB)	Infer. (ms)
U-Net	31.0	124.0	–
UNet++	9.0	36.0	–
TransUNet	93.0	372.0	–
U-KAN	14.0	56.0	–
RadiomicNet	3.27	13.1	8.85

learning paradigm that is simultaneously more parameter-efficient, more interpretable, and competitive in performance. This aligns directly with the LBDL vision: the model’s decision process is traceable to mathematically defined, clinically validated features rather than abstract neural activations.

The Radiomics Consistency Loss introduces a soft inductive bias derived from clinical knowledge (texture complexity correlates with diagnostic uncertainty), embedding radiological reasoning into the training objective rather than appending it post-hoc. The demonstrated ECE reduction (0.142 to 0.118) confirms that this constraint is not a marginal regulariser but a meaningful calibration mechanism.

Limitations. The current radiomics feature set is fixed at 13 features; future work could learn an optimal radiomics subset via differentiable feature selection. The model currently processes 2D slices; extension to 3D volumes for CT/MRI modalities is planned. Evaluation on additional modalities (CT, MRI) remains a direction for future work.

VI. CONCLUSION

We presented RadiomicNet, a two-stream hybrid architecture that integrates handcrafted radiomics texture features into a lightweight segmentation network through the novel Radiomics Attention Gate. By embedding clinical knowledge directly into the attention mechanism and loss function, RadiomicNet achieves ante-hoc interpretability — not as an afterthought, but as a structural property. With 3.27M parameters, 13.1 MB model size, statistically significant DSC improvements ($p < 0.05$) across two medical imaging modalities, and demonstrated calibration improvement (ECE: 0.142 \rightarrow 0.118), RadiomicNet offers a viable path toward interpretable, edge-deployable clinical AI that goes *beyond deep learning*.

REFERENCES

- [1] O. Ronneberger, P. Fischer, and T. Brox, “U-Net: Convolutional networks for biomedical image segmentation,” in *Proc. MICCAI*, 2015, pp. 234–241.
- [2] Z. Zhou, M. M. R. Siddiquee, N. Tajbakhsh, and J. Liang, “UNet++: A nested U-Net architecture for medical image segmentation,” in *Deep Learning in Medical Image Analysis*, 2018, pp. 3–11.
- [3] J. Chen *et al.*, “TransUNet: Rethinking the U-Net architecture design for medical image segmentation through the lens of transformers,” *Medical Image Analysis*, vol. 97, 2024.
- [4] C. Li, X. Liu, W. Li, C. Wang, H. Liu, and Y. Yuan, “U-KAN makes strong backbone for medical image segmentation and generation,” in *Proc. AAAI*, 2025, pp. 4652–4660.
- [5] M. Chen, J. Zhang, L. Jin, X. Xuan, and Y. Cheng, “IKANet: A Kolmogorov-Arnold network for interpretable medical image segmentation,” in *Proc. PRCV*, 2025.
- [6] Z. Liu *et al.*, “KAN: Kolmogorov-Arnold networks,” in *Proc. ICLR*, 2025.
- [7] P. Lambin *et al.*, “Radiomics: Extracting more information from medical images using advanced feature analysis,” *Eur. J. Cancer*, vol. 48, no. 4, pp. 441–446, 2012.
- [8] R. J. Gillies, P. E. Kinahan, and H. Hricak, “Radiomics: Images are more than pictures, they are data,” *Radiology*, vol. 278, no. 2, pp. 563–577, 2016.
- [9] S. Basu *et al.*, “Focus on texture: Rethinking pre-training in masked autoencoders for medical image classification,” in *Proc. MICCAI*, 2025.
- [10] B. Baidya Kayal *et al.*, “Advances in medical image segmentation: A comprehensive review of traditional, deep learning and hybrid approaches,” *Bioengineering*, vol. 11, no. 10, 2024.
- [11] W. Al-Dhabyani, M. Gomaa, H. Khaled, and A. Fahmy, “Dataset of breast ultrasound images,” *Data in Brief*, vol. 28, 2020.
- [12] D. Jha *et al.*, “Kvasir-SEG: A segmented polyp dataset,” in *Proc. MMM*, 2020, pp. 451–462.
- [13] M. Sandler, A. Howard, M. Zhu, A. Zhmoginov, and L.-C. Chen, “MobileNetV2: Inverted residuals and linear bottlenecks,” in *Proc. CVPR*, 2018.
- [14] C.-C. J. Kuo and L. Guan, “The second workshop on learning beyond deep learning (LBDL II),” in *Proc. IEEE ICIP Workshop*, 2026.